



Achieving tunable photocatalytic activity enhancement by elaborately engineering composition-adjustable polynary heterojunctions photocatalysts

Chao Zeng^a, Yingmo Hu^{a,*}, Yuxi Guo^a, Tierui Zhang^b, Fan Dong^c, Xin Du^d, Yihe Zhang^a, Hongwei Huang^{a,*}

^a Beijing Key Laboratory of Materials Utilization of Nonmetallic Minerals and Solid Wastes, National Laboratory of Mineral Materials, School of Materials Science and Technology, China University of Geosciences, Beijing 100083, China

^b Key Laboratory of Photochemical Conversion and Optoelectronic Materials, Technical Institute of Physics and Chemistry, Chinese Academy of Sciences, Beijing 100190, China

^c Chongqing Key Laboratory of Catalysis and Functional Organic Molecules, College of Environmental and Biological Engineering, Chongqing Technology and Business University, Chongqing, 400067, China

^d Research Center for Bioengineering and Sensing Technology, Department of Chemistry & Biological Engineering, University of Science & Technology Beijing, Beijing 100083, China

ARTICLE INFO

Article history:

Received 16 February 2016

Received in revised form 13 April 2016

Accepted 16 April 2016

Available online 19 April 2016

Keywords:

Photocatalyst
Composition-adjustable
Three-classes
 $\text{Bi}_7\text{O}_9\text{I}_3/\text{AgI}/\text{AgI}\text{O}_3$
Simulated solar light

ABSTRACT

We first achieve controllable synthesis of composition-adjustable polynary heterojunction photocatalysts *via* a facile *in-situ* treatment strategy at ambient conditions based on component transformation and chemical deposition. By controlling the chemical reaction degree, three-classes of heterojunction composites with diverse components were produced. The first group (G1) contains $\text{AgI}/\text{AgI}\text{O}_3$ two phases. The second group (G2) consists of $\text{Bi}_7\text{O}_9\text{I}_3/\text{AgI}/\text{AgI}\text{O}_3$ three phases. While the last group (G3) is composed of $\text{Bi}_7\text{O}_9\text{I}_3/\text{AgI}$. Along with different phase constitution, it is very intriguing to observe that photoabsorption edges of the composites can be orderly tuned from 400 nm to 650 nm, covering almost the whole visible light region, consistent with the color change of samples from white to light yellow, orange and brick red. The three series of composite photocatalysts all show greatly enhanced photocatalytic activity in photodegrading methyl orange (MO) and NO gas removal under simulated solar light or visible light irradiation compared with the AgIO_3 precursor. Among them, the intense photoabsorption and desirable band alignment (three-rank heterojunction) are well balanced in $\text{Bi}_7\text{O}_9\text{I}_3/\text{AgI}/\text{AgI}\text{O}_3$, thus showing the optimal photoreactivity, approximately 128 times than that of AgIO_3 . Particularly, it also exhibits unsurpassed photocatalytic performance against diverse industrial pollutants and pharmaceutical, such as Rhodamine B, phenol, 2,4-dichlorophenol, bisphenol A, and tetracycline hydrochloride. Additionally, three types of photocatalytic mechanisms corresponding to the three series of photocatalysts are systematically investigated and illustrated. It is found that different phase composition has a huge impact on the separation and migration of charges as well as active species. The present work not only provides new perspective into manipulating component-adjustable heterojunctional photocatalysts, but also opens an alternative avenue for developing composite materials for solar-conversion applications.

© 2016 Elsevier B.V. All rights reserved.

1. Introduction

Photocatalysis technology has drawn great attention because of its huge potentials in degradation of organic contamination, NO removal from air, CO_2 conversion, and hydrogen evolution

[1–3]. Whereas, lots of current semiconductors still cannot be practically applied due to their weak utilization efficiency of visible light and/or high recombination rate of holes and electrons [4–7]. In general, heterojunctional photocatalysts that consist of wide-band-gap semiconductors and narrow-band-gap semiconductors with band structure alignment and intimate interfacial interaction exhibit high photoabsorption and photogenerated charge separation, thus possess excellent visible-light photocatalytic activity [8,9]. Therefore, researchers are devoted to developing various het-

* Corresponding authors.

E-mail addresses: huyingmo@cugb.edu.cn (Y. Hu), [\(H. Huang\).](mailto:hhw@cugb.edu.cn)

erojunctional structures to promote the visible light absorption and photocatalytic activity of semiconductors.

Since the photocatalytic activity is closely associated with the components in heterojunctions, fabrication of heterostructural photocatalysts that contains multiple active components is desirable. Nonetheless, up to now, the fabrication of multiple-components heterostructural photocatalysts is very tedious and time consuming. For example, Ag/AgBr/AgVO₄ [10], Ag/AgCl/BiVO₄ [11], Ag/AgCl/C₃N₄ [12], and Ag/Ag₃PO₄/g-C₃N₄ [13] multiplex composite photocatalysts were all prepared through multi-step process with complex procedures, which seriously restricted their practical application. Therefore, it is very significant to exploit facile method to synthesize multiplex heterostructure photocatalysts.

Recently, non-metal oxy-acid salts are believed to be a promising source for developing novel photocatalysts with excellent photocatalytic performance for organic pollutant removal. Among them, particularly, iodates exhibit outstanding photocatalytic ability. Because the (IO₃)⁻ anion group with a long pair electrons of I⁵⁺ can polarize crystals to form layered structure, which greatly facilitates the separation of electrons and holes. The iodate photocatalysts, such as Ln(IO₃)₃ (Ln = Ce, Nd, Eu, Gd, Er, Yb) [14], Y(IO₃)₃ [15], Bi(IO₃)₃ [16], and Bi₂O₄ [17], all possess superior photocatalytic performance for azo dye photodegradation under ultraviolet light illumination. Therefore, iodates can be served as a potential candidate for new generation photocatalysts. Recently, AgIO₃, a layered iodate photocatalyst, was found to effectively photodecompose dye [18] and reduce CO₂ to CH₄ and CO [19]. However, the visible light absorption of AgIO₃ is relatively weak. Constructing heterostructure can be used to enhance the absorption in visible light region and restrain hole-electrons recombination of AgIO₃. Furthermore, compared with other silver-containing semiconductors (such as Ag₃PO₄ [20], Ag₂CO₃ [21], Ag₃VO₄ [22], etc.), there are two kinds of redox-couple components Ag/Ag⁺ and (IO₃)⁻/I⁻ in AgIO₃. So it may be viable to fabricate AgIO₃-based heterojunctions based on redox reactions. In recent years, it was corroborated that the silver halide (AgX, X = Cl, Br, I) was a type of promising visible-light driven photocatalyst for degradation of various dyes [23]. Among the AgX group, AgI exhibits the highest photocatalytic activity in contrast to AgCl and AgBr, because I⁻ reacts with photogenerated holes (h_{VB}⁺) faster than Cl⁻ and Br⁻ [24]. In addition, bismuth oxyhalides, a new family of V-VI-VII ternary oxides, including BiOX (X = Cl, Br, I) [25] and Bi₄O₅I₂ [26], Bi₇O₉I₃ [27], Bi₅O₇I [28], exhibit great promise. Benefiting from their distinctive layered crystal structure with an internal static electric field perpendicular to each layer [29], which can facilitate the separation of photoinduced electron-hole pairs, enabling bismuth oxyhalides to show superior photocatalytic and photoelectrochemical performances. Among these bismuth oxyhalides, Bi₇O₉I₃ exhibits the best photocatalytic activity in decomposition of dyes under visible light irradiation [30]. However, there is merely an article reporting the heterostructure photocatalyst containing Bi₇O₉I₃ (Bi₇O₉I₃/Bi₂O₂CO₃) [31], in which it shows excellent photocatalytic activity for phenol degradation under visible light illumination ($\lambda > 400$ nm). Thereby, it is feasible to employ AgI and Bi₇O₉I₃ to enhance the visible light absorption and photocatalytic capability of AgIO₃.

Herein, we elaborately engineer multi-class heterojunction composite photocatalysts by utilizing AgIO₃ as the self-sacrifice precursor *via* a facile *in-situ* reaction at room temperature. Through simply controlling the Bi(NO₃)₃·5H₂O and KI concentration, the phase component of composite can be interestingly adjusted, resulting in three classes of heterojunctions, namely AgI/AgIO₃, Bi₇O₉I₃/AgI/AgIO₃ and Bi₇O₉I₃/AgI. With the change of phase composition, the photoresponsive range of composite is orderly tuned, almost covering the whole visible light region. To reveal the difference of phase composition in photo-activity, the photocatalytic

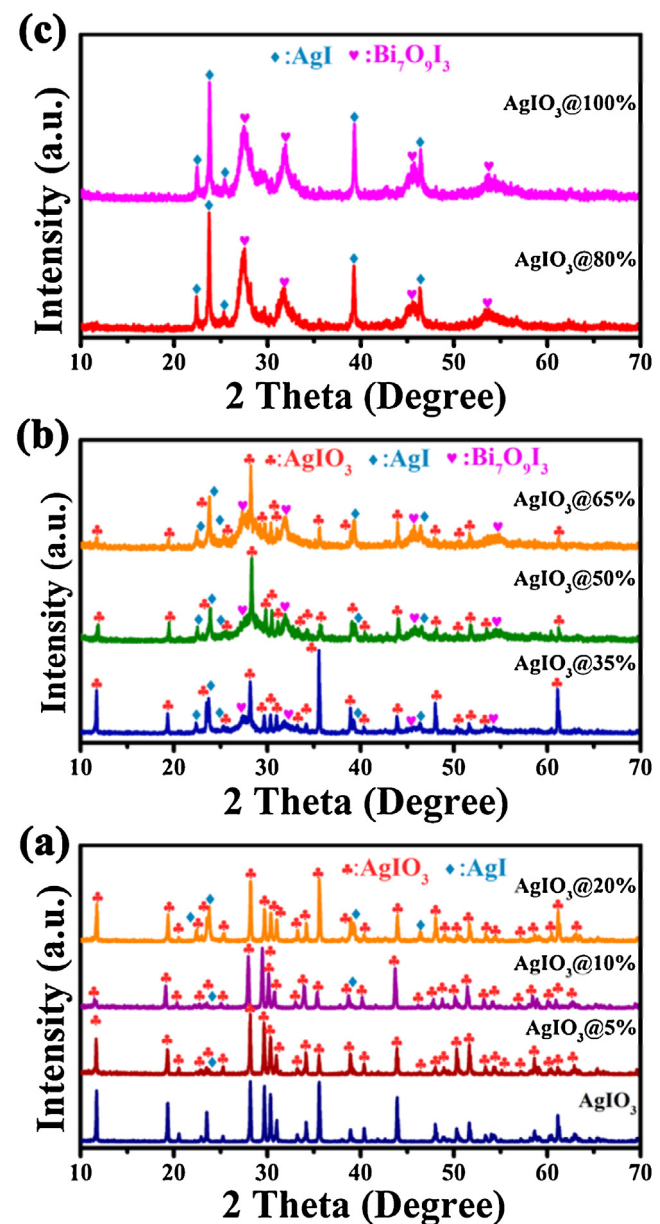


Fig. 1. XRD patterns for (a) pure AgIO₃, G1 samples (AgIO₃@5%, AgIO₃@10%, AgIO₃@20%), (b) G2 samples (AgIO₃@35%, AgIO₃@50%, AgIO₃@65%), and (c) G3 samples (AgIO₃@80%, AgIO₃@100%).

properties are systematically tested by the decomposition of multiple industrial contaminants and pharmaceutical, including methyl orange (MO), Rhodamine B (RhB), phenol, 2,4-Dichlorophenol (2,4-DCP), tetracycline hydrochloride, bisphenol A (BPA), and NO in gaseous phase. Besides, the diverse photocatalytic mechanisms corresponding to different heterojunction are detailedly studied by multiple techniques. This work may pave a new way for manufacturing more desired heterojunctional materials with excellent photochemical performance.

2. Experimental

2.1. Preparation of the photocatalyst

All starting materials used were analytical grade. AgIO₃ precursor was prepared *via* a hydrothermal method. Typically, 2 mmol AgNO₃ and 1 mmol I₂O₅ were dispersed in 40 ml of deionized water

with ultrasonic to obtain a homogeneous suspension. Then the resultant suspension was transferred to a Teflon-lined autoclave with a capacity of 50 ml and heated at 180 °C for 24 h. After natural cooling to room temperature, the product was filtrated, washed, and then dried at 80 °C for 10 h in air.

The composites photocatalysts were fabricated by a facile *in-situ* reaction. Briefly, 1 mmol AgI_{0.3} precursor and quantitative Bi(NO₃)₃·5H₂O with the Bi(NO₃)₃·5H₂O/AgI_{0.3} molar ratios of X (X=5%, 10%, 20%, 35%, 50%, 65%, 80%, and 100%) were ultrasonically dispersed in 20 ml glycol. Stoichiometric amounts of KI, which is equal to the molar amount of Bi(NO₃)₃·5H₂O, was dissolved in 20 ml deionized water and then added into the above AgI_{0.3} and Bi(NO₃)₃·5H₂O suspension under stirring step by step. Subsequently, the suspension was drastically magnetic stirred for 1 h at room temperature. The product was filtrated, washed with distilled water and ethanol, then dried at 80 °C overnight. The composite photocatalysts with different X values (X=5%, 10%, 20%, 35%, 50%, 65%, 80%, and 100%) were obtained, and marked as AgI_{0.3}@5%, AgI_{0.3}@10%, AgI_{0.3}@20%, AgI_{0.3}@35%, AgI_{0.3}@50%, AgI_{0.3}@65%, AgI_{0.3}@80%, and AgI_{0.3}@100%, respectively. The schematic illustration for the formation of AgI_{0.3}@X sample is displayed in [Scheme 1](#). The as-prepared samples can be divided into three groups on the basis of their component, namely, the first group (marked as G1), including AgI_{0.3}@X (X=5%, 10%, 20%), which contains AgI_{0.3}, AgI phases, and the second group (marked as G2), including AgI_{0.3}@X (X=35%, 50%, 65%), consists of AgI_{0.3}, AgI, and Bi₇O₉I₃ three phases, and the third group (marked as G3), including AgI_{0.3}@X (X=80%, 100%), is composed of AgI and Bi₇O₉I₃, respectively. The formation of different phases is detailedly discussed in the following.

2.2. Characterization

X-ray powder diffraction (XRD) was evaluated by a Bruker D8 focus with Cu K α radiation (40 kV/40 mA). An ESCALAB 250xi (ThermoFisher, England) electron spectrometer was used to measure the X-ray photoelectron spectroscopy (XPS). Scanning electron microscopy (SEM) and transmission electron microscopy (TEM) were identified on Hitachi S-4800 and JEM-2100, respectively. UV-vis diffuse reflectance spectra (DRS) were carried out by a Varian Cary 5000 UV-vis spectrophotometer. The photoluminescence spectra were performed on a Hitachi F-4600 fluorescence spectrophotometer taking a xenon lamp as an excitation source. All the measurements were obtained at room temperature.

2.3. Photocatalytic activity

The photocatalytic activities of composites photocatalysts were tested by photocatalytic degradation of various water pollutants, including Methyl Orange (MO, 1*10⁻⁵ mol/L), Rhodamine B (RhB, 2 × 10⁻⁵ mol/L), bisphenol A (BPA, 10 mg/L), tetracycline hydrochloride (10 mg/L), phenol (20 mg/L), 2,4-dichlorophenol (2,4-DCP, 20 mg/L), under simulated solar light or visible light ($\lambda > 420$ nm) irradiation. A total of 20 mg photocatalyst was ultrasonically dispersed in 40 ml pollutant aqueous solution. Before photoreaction, the suspensions in quartz tubes were magnetically stirred in dark for 30 min to get an adsorption-desorption equilibrium between photocatalyst and aqueous solution. After illumination, about 3 ml of the liquid was extracted from each sample at certain period time, and centrifuged to get the supernatant. The concentration of pollutant aqueous solution was analyzed by monitoring the absorbance on a Cary 5000 UV-vis spectrophotometer.

Removal of NO at ppb levels at ambient temperature was also employed to investigate the photocatalytic activity. A 150 W commercial tungsten halogen lamp (without filter) was used as light

source. Photocatalyst (0.15 g) was dispersed in 50 ml deionized water. After ultrasonic for 10 min, the suspension was coated onto a dish (12.0 cm in diameter). Then, the coated dish was pretreated at 70 °C. The initial 450 ppb NO gas in the measurement was acquired by diluted 100 ppm of NO gas from a compressed gas cylinder with flowing air. After getting adsorption-desorption equilibrium, the concentrations of NO_x (NO and NO₂) were measured by a NO_x analyzer (Thermo Scientific, 42i-TL) in the interval of every minute, so the concentration of NO can be determined.

2.4. Active species trapping experiment

Generally, during the photocatalytic process, several kinds of active species, including hydroxyl radical (·OH), hole (h⁺), and superoxide radical (·O₂⁻), would generate. To detect the active species produced in the photodecomposition process of MO, another MO photodegradation experiment was carried out with the addition of 1 mM *tert*-butyl alcohol (TBA)/1 mM ethylene glycol (IPA), 1 mM disodium ethylenediaminetetraacetate (EDTA-2Na)/1 mM ammonium oxalate (AO) and 1 mM benzoquinone (BQ) to scavenge ·OH, h⁺, and ·O₂⁻, respectively.

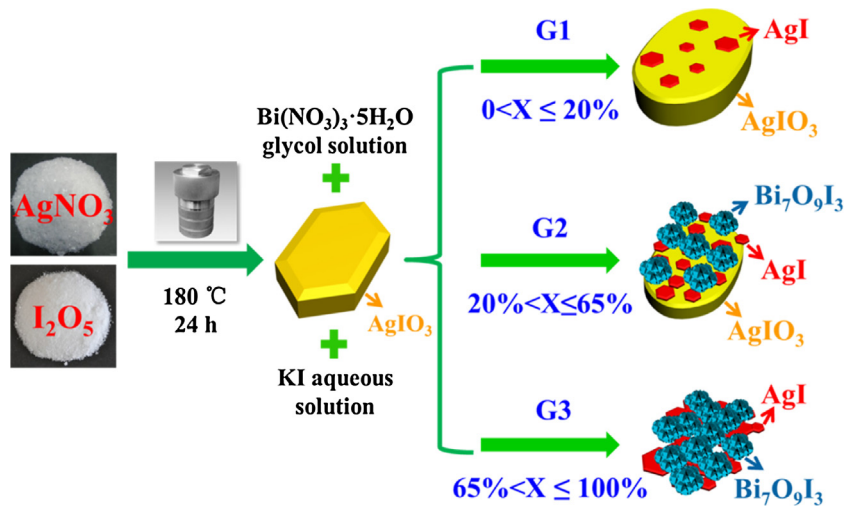
2.5. Photoelectrochemical measurement

The photoelectrochemical measurements, including electrochemical impedance spectra (EIS) and Mott–Schottky curve, were conducted on an electrochemical analyzer (CHI660E, Shanghai) equipped with a standard three-electrode system. Platinum (Pt) wire is the counter electrode and saturated calomel electrodes (SCE) serve as a reference electrode. The light source is a 300W Xe arc lamp (without filter). The electrolyte solution was Na₂SO₄ (0.1 M) aqueous solution. The working electrode was the AgI_{0.3}, AgI_{0.3}@20% (AgI/AgI_{0.3}), AgI_{0.3}@65% (Bi₇O₉I₃/AgI/AgI_{0.3}) and AgI_{0.3}@100% (Bi₇O₉I₃/AgI) sample films coated on ITO.

3. Results and discussion

3.1. Structure and morphology

The XRD patterns of the as-prepared composite photocatalysts AgI_{0.3}@X (X=5%, 10%, 20%, 35%, 50%, 65%, 80%, 100%) are displayed in [Fig. 1](#). The diffraction peaks of pure AgI_{0.3} match well with AgI_{0.3} standard data (ICSD#14100), and all the composite photocatalysts contain AgI phase according to the standard pattern of AgI (JCPDS#1-520). When the X value reaches 35%, a broad peak centering at about 28.4° appears, which can be ascribed to Bi₇O₉I₃ on the basis of previous report [32]. In addition, when X is 80% or 100%, the diffraction peaks of AgI_{0.3} can no longer be found. Thus, the as-obtained composite photocatalysts can be divided into three groups (G1, G2, and G3) based on their different components. The G1 samples ([Fig. 1a](#)), including AgI_{0.3}@X (X=5%, 10%, 20%), consist of AgI/AgI_{0.3} phases. The G2 samples ([Fig. 1b](#)), including AgI_{0.3}@X (X=35%, 50%, 65%), are composed of Bi₇O₉I₃/AgI/AgI_{0.3} three phases. As for the G3 samples ([Fig. 1c](#)), including AgI_{0.3}@X (X=80%, 100%), are mainly composed of Bi₇O₉I₃/AgI. To better illustrate the formation of AgI_{0.3}@X samples, we display their formation process in [Scheme 1](#). It can be concluded that KI first reacts with AgI_{0.3} instead of Bi(NO₃)₃·5H₂O through ion-exchange to produce AgI when the addition amount of KI is small. So the samples in G1 do not contain Bi₇O₉I₃. When KI amount is enough, namely X beyond 20%, KI starts to react with Bi(NO₃)₃·5H₂O to generate Bi₇O₉I₃, which appears in samples of G2. When X increases to 80%, the KI amount is too high and AgI_{0.3} is exhausted, resulting in the appearance of only two phases of AgI and Bi₇O₉I₃ in G3. Therefore, the fabrication of component-adjustable multiplex heterostructure



Scheme 1. Schematic illustration for the formation of AgI_3 precursor and three groups (G1, G2, and G3) samples.

photocatalysts is realized by simply controlling the KI concentration.

To investigate the chemical situation of each atom, X-ray photoelectron spectroscopy (XPS) of the three kinds of composite photocatalysts $\text{AgI}_3@20\%$ (AgI/AgI_3), $\text{AgI}_3@65\%$ ($\text{Bi}_7\text{O}_9\text{I}_3/\text{AgI}/\text{AgI}_3$), and $\text{AgI}_3@100\%$ ($\text{Bi}_7\text{O}_9\text{I}_3/\text{AgI}$) is conducted. As shown in Fig. 2a, the characteristic peaks of component elements Bi 4f, I 3d, O 1s, and Ag 3d can be observed in spectra of $\text{AgI}_3@65\%$ and $\text{AgI}_3@100\%$, meanwhile the spectrum of $\text{AgI}_3@20\%$ is lack of Bi 4f compared to two other spectra. The C peak is resulted from the residual carbon of the XPS instrument. From the high resolution XPS spectra of Bi (Fig. 2b), it is obvious that $\text{AgI}_3@20\%$ sample does not contain Bi atoms, which is consistent with the XRD result that $\text{AgI}_3@20\%$ sample does not contain $\text{Bi}_7\text{O}_9\text{I}_3$ phase. Moreover, there is almost no shift for the binding energies of Bi $4f_{5/2}$ and Bi $4f_{3/2}$ at about 164.4 eV and 159.1 eV in $\text{AgI}_3@65\%$ and $\text{AgI}_3@100\%$, suggesting that the chemical situation of bismuth in the two samples is similar [33]. The high resolution XPS spectrum for I is depicted in Fig. 2c. For $\text{AgI}_3@20\%$, four strong peaks at 620.3 , 624.3 , 631.7 , and 635.9 eV can be found, which are ascribed to $\text{I}^- 3d_{5/2}$, $\text{I}^{5+} 3d_{5/2}$, $\text{I}^- 3d_{3/2}$, and $\text{I}^{5+} 3d_{3/2}$, respectively [34]. For $\text{AgI}_3@65\%$ and $\text{AgI}_3@100\%$, the four peaks can be deconvoluted into six peaks. In $\text{AgI}_3@65\%$, peaks at 620.1 , 624.1 , 631.5 and 635.5 eV are attributed to I^- , I^{5+} , I^- , and I^{5+} , while the two new peaks at 619.5 and 630.8 eV can be assigned to $\text{I} 3d$ in $\text{Bi}_7\text{O}_9\text{I}_3$ [35]. In $\text{AgI}_3@100\%$, peaks with binding energies at 620.7 , 624.1 , 631.6 and 635.5 eV are ascribed to I^- , I^{5+} , I^- , and I^{5+} , and simultaneously the other peaks centering at 619.7 and 631.1 eV are due to I atoms in $\text{Bi}_7\text{O}_9\text{I}_3$. The peaks of I^{5+} in $\text{AgI}_3@100\%$ indicate the existence of AgI_3 . However, the distinct diffraction peak for AgI_3 in the $\text{AgI}_3@100\%$ XRD pattern cannot be found. Therefore, it can be inferred that the amount of AgI_3 in $\text{AgI}_3@100\%$ sample is very small and can be neglected. In addition, for $\text{AgI}_3@20\%$, the characteristic peak of I in $\text{Bi}_7\text{O}_9\text{I}_3$ is not visible, further corroborating the inexistence of $\text{Bi}_7\text{O}_9\text{I}_3$ in $\text{AgI}_3@20\%$. The high resolution XPS spectra for O 1s of $\text{AgI}_3@X$ ($X = 20\%$, 65% , 100%) are portrayed in Fig. 2d. With increasing the X value, the O 1s peak shifts to low binding energy. It is reasonable because $\text{Bi}_7\text{O}_9\text{I}_3$ appears in $\text{AgI}_3@65\%$ and $\text{AgI}_3@100\%$, and the chemical environment of oxygen atoms in $\text{Bi}_7\text{O}_9\text{I}_3$ is different from that in AgI_3 . The XPS conclusions are coincident with the XRD results, revealing that the components of samples in three groups (G1, G2, and G3) are different.

The morphology and structure of the as-prepared samples are investigated by scanning electron microscopy (SEM), energy

dispersive X-ray (EDX), and EDX mapping, as shown in Fig. 3. From Fig. 3a–d, one can see that the pure AgI_3 is spindle-like with sharp corners, and the diameter is about $2\text{--}5\text{ }\mu\text{m}$. With increasing the X value of $\text{AgI}_3@X$, the sharp corners of AgI_3 disappear. When $X = 20\%$ (belong to G1), some nanosheets emerge at the surface of AgI_3 (Fig. 3b), which are concluded to be AgI according to the XRD result. With increasing X to 65% (belong to G2), some flower-like microspheres also appear besides AgI nanosheets (Fig. 3c), which are believed to be $\text{Bi}_7\text{O}_9\text{I}_3$. Until $X = 100\%$ (belong to G3), the AgI_3 precursor cannot be found, most of which have converted to AgI via the reaction between AgI_3 and KI, as shown in Fig. 3d and Fig. S1. Schematic illustration for morphology change of AgI_3 , $\text{AgI}_3@20\%$ (G1, AgI/AgI_3), $\text{AgI}_3@100\%$ (G2, $\text{Bi}_7\text{O}_9\text{I}_3/\text{AgI}/\text{AgI}_3$), and $\text{AgI}_3@100\%$ (G3, $\text{Bi}_7\text{O}_9\text{I}_3/\text{AgI}$) photocatalysts was exhibited in Fig. 3e. EDX is carried out to further manifest the co-existence of AgI_3 , AgI and $\text{Bi}_7\text{O}_9\text{I}_3$ in $\text{AgI}_3@65\%$ composite (Fig. 3f). The Be element is used as a contrast, and the signal of Al and Pt are attributed to the carrier of aluminum foil and the process of gilding. It is obvious to observe three phases with different morphologies. The main part is detected to be AgI_3 , and the nanosheets are AgI . With regard to the flower-like microspheres, the atom ratio of Bi: O: I is $8.03\%: 11.2\%: 3.58\%$ on the basis of EDX result. So the flower-like materials can be concluded to be $\text{Bi}_7\text{O}_9\text{I}_3$ combining the XRD results. Therefore, it is confirmed that the $\text{AgI}_3@65\%$ sample (belong to G2) consists of AgI_3 , AgI , and $\text{Bi}_7\text{O}_9\text{I}_3$ three phases. Moreover, the EDX mapping (Fig. 3g–j) reveals that the Ag, I, O and Bi elements are uniformly distributed in the $\text{AgI}_3@65\%$ sample. It can be deduced from the results of XRD, SEM and EDX that the composition of the product is tunable with controlling the value of X in $\text{AgI}_3@X$.

To further explore the microstructure of $\text{AgI}_3@65\%$ (belong to G2), TEM and HRTEM images are depicted in Fig. 4. It can be found from Fig. 4a,b and Fig. S2 that the AgI nanoplates and $\text{Bi}_7\text{O}_9\text{I}_3$ microspheres surround the AgI_3 cores. According to Fig. 4c, four distinct regions with different fringe spaces can be distinguished. Two lattice fringes with intervals of 0.35 and 0.26 nm can be assigned to the AgI_3 crystal. The adjacent fringes with distance of 0.34 nm coincide well with the (101) lattice of AgI on the basis of the JCPDS#1-520 card information. The fringes with interval of 0.32 nm may be attributed to the crystal facet of $\text{Bi}_7\text{O}_9\text{I}_3$ corresponding to its strong diffraction peak at 28.4° [27]. Consequently, AgI_3 , AgI , and $\text{Bi}_7\text{O}_9\text{I}_3$ are detected in $\text{AgI}_3@65\%$ through TEM images, and meanwhile the three phases closely contact each other, which would facilitate the separation and transfer of photogenerated charges.

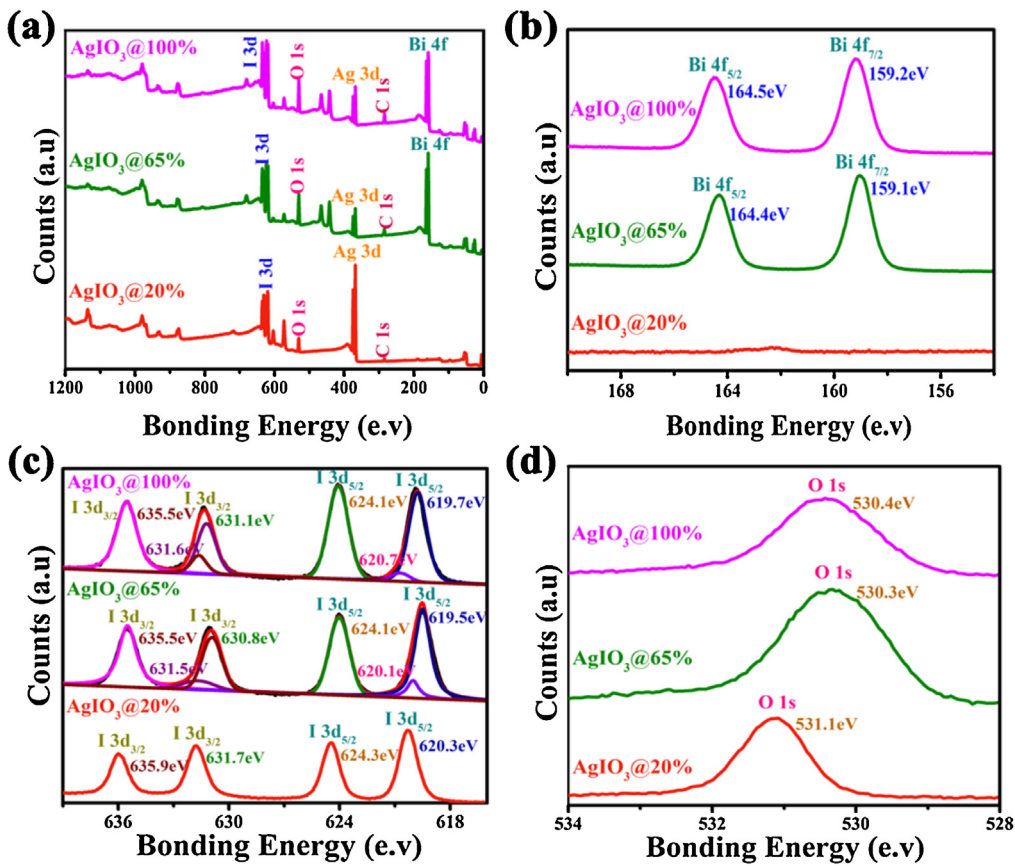


Fig. 2. Typical XPS survey spectra (a), high-resolution XPS spectrum for Bi (b), I (c), and O (d) of AgIO_3 @20% (G1, AgI/AgIO_3), AgIO_3 @65% (G2, $\text{Bi}_7\text{O}_9\text{I}_3/\text{AgI}/\text{AgIO}_3$), AgIO_3 @100% (G3, $\text{Bi}_7\text{O}_9\text{I}_3/\text{AgI}$).

3.2. Light absorption adjusting

Diffuse reflection spectroscopy (DRS) is employed to survey light absorption property of the as-obtained photocatalysts. As shown in Fig. 5, the absorption edge of AgIO_3 locates at about 380 nm, which is consistent with the reported value [18]. Amazingly, all the as-prepared three-groups products $\text{AgIO}_3@X$ ($X=5\%, 10\%, 20\%, 35\%, 50\%, 65\%, 80\%, 100\%$) exhibit greatly enhanced visible-light absorption compared to pure AgIO_3 , and the photoabsorption range is gradually extended from AgIO_3 to G1, G2 and G3. In particular, it should be noted that the spectra of G1 samples with absorption edge at about 460 nm, including $\text{AgIO}_3@X$ ($X=5\%, 10\%, 20\%$), are similar, reflecting the composition of the three samples are the same. The enhancement in their visible-light absorption is attributed to the generation of AgI . The spectra of samples in other two groups (G2 and G3), including $\text{AgIO}_3@X$ ($X=35\%, 50\%, 65\%, 80\%, 100\%$), exhibit a strongly enhanced visible-light absorption, which should be due to the existence of $\text{Bi}_7\text{O}_9\text{I}_3$. And the absorption edges of the G2 and G3 composites are further extended to 600 and 650 nm, respectively. Furthermore, from the digital photos of the AgIO_3 , $\text{AgIO}_3@20\%$ (AgI/AgIO_3), $\text{AgIO}_3@65\%$ ($\text{Bi}_7\text{O}_9\text{I}_3/\text{AgI}/\text{AgIO}_3$), and $\text{AgIO}_3@100\%$ ($\text{Bi}_7\text{O}_9\text{I}_3/\text{AgI}$) samples, it can be observed that the color of samples gradually changes from white to light yellow, orange and brick red, consistent with the change of the photoabsorption and composition.

The band gap of AgIO_3 can be evaluated by the following Kubelka-Munk equation [36]: $\alpha h\nu = (\alpha h\nu - E_g)^n$, here h , α , v , A , and E_g represents the Planck's constant, optical absorption coefficient, photon frequency, a constant, and photonic energy band gap, respectively. For AgIO_3 , an indirect-transition allowed semi-

conductor with $n=2$, the E_g of AgIO_3 is estimated to be 3.18 eV, as shown in Fig. S3.

3.3. Photocatalytic activity enhancement

3.3.1. Photodegradation of MO

The photocatalytic activity of as-prepared AgIO_3 and the three classes of composite photocatalysts are first evaluated by photodegradation of MO under simulated solar light irradiation. Photodegradation curves of MO solution over the AgIO_3 , and $\text{AgIO}_3@X$ ($X=5\%, 10\%, 20\%, 35\%, 50\%, 65\%, 80\%, 100\%$) are illustrated in Fig. 6a. Without catalyst, very little MO could be degraded after simulated solar light irradiation for 50 min, which can be neglected. It can be found that all the composite photocatalysts ($\text{AgIO}_3@X$) exhibit better photocatalytic activity than the pristine AgIO_3 . Particularly, upon increasing the X value from 20% to 35%, the photocatalytic activity of samples has been rapidly strengthened, which should be ascribed to the generation of $\text{Bi}_7\text{O}_9\text{I}_3$. In addition, the $\text{AgIO}_3@X$ ($X=35\%, 50\%, 65\%, 80\%, 100\%$) in G2 and G3, which contain $\text{Bi}_7\text{O}_9\text{I}_3$, all exhibit markedly stronger photocatalytic activity than the $\text{AgIO}_3@X$ ($X=5\%, 10\%, 20\%$) samples in G1. All these samples in G2 and G3 can remove more than 98% of MO after 50 min simulated solar light irradiation. Whereas, the $\text{AgIO}_3@20\%$ which shows the best photocatalytic activity in G1 ($\text{AgIO}_3@5\%$, $\text{AgIO}_3@10\%$, $\text{AgIO}_3@20\%$) can only degrade 61% of MO. The photodegradation rate constants of all the as-obtained photocatalysts are shown in Fig. 6b. The reaction rate constant of the MO photodegradation process in quantitative terms are calculated by the following pseudo-first-order equation [37]: $\ln(C_0/C) = k_{app}t$, where k_{app} , C_0 , C represent the rate constant (min^{-1}), initial MO solution concentration (mol/L), and instantaneous MO solution

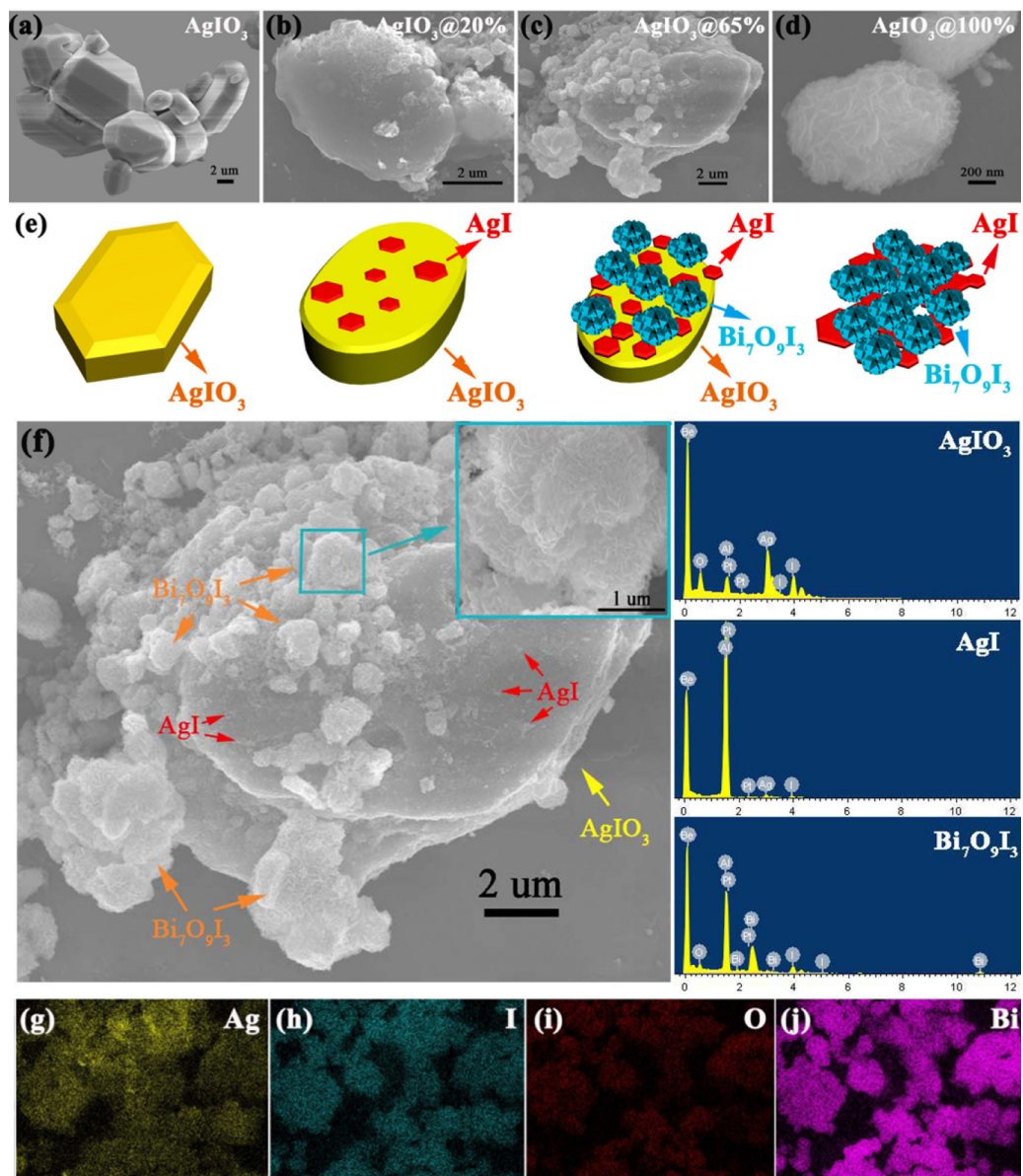


Fig. 3. SEM images of AgIO_3 (a), $\text{AgIO}_3@20\%$ (G1, AgI/AgIO_3) (b), $\text{AgIO}_3@65\%$ (G2, $\text{Bi}_7\text{O}_9\text{I}_3/\text{AgI}/\text{AgIO}_3$) (c), $\text{AgIO}_3@100\%$ (G3, $\text{Bi}_7\text{O}_9\text{I}_3/\text{AgI}$) (d), Schematic illustration of morphology change for AgIO_3 and $\text{AgIO}_3@X$ ($X=20\%, 65\%, 100\%$) products (e), SEM and EDX images for the $\text{AgIO}_3@65\%$ (f), EDX mapping of $\text{AgIO}_3@65\%$ (g–j).

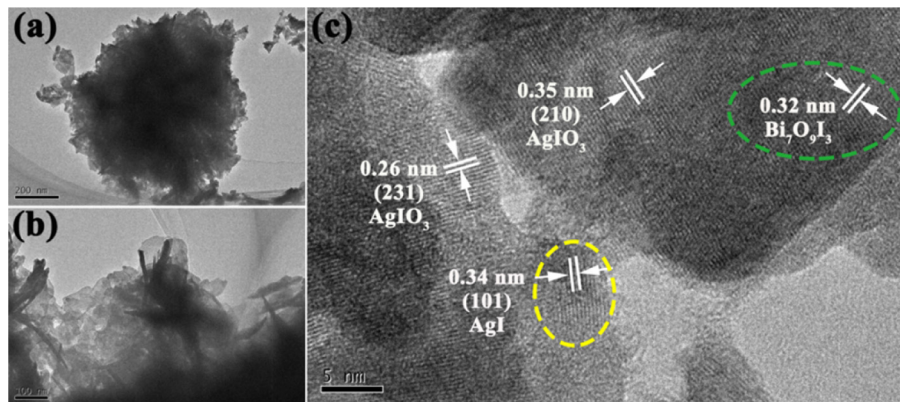


Fig. 4. TEM and HRTEM images of $\text{AgIO}_3@65\%$ (G2, $\text{Bi}_7\text{O}_9\text{I}_3/\text{AgI}/\text{AgIO}_3$).

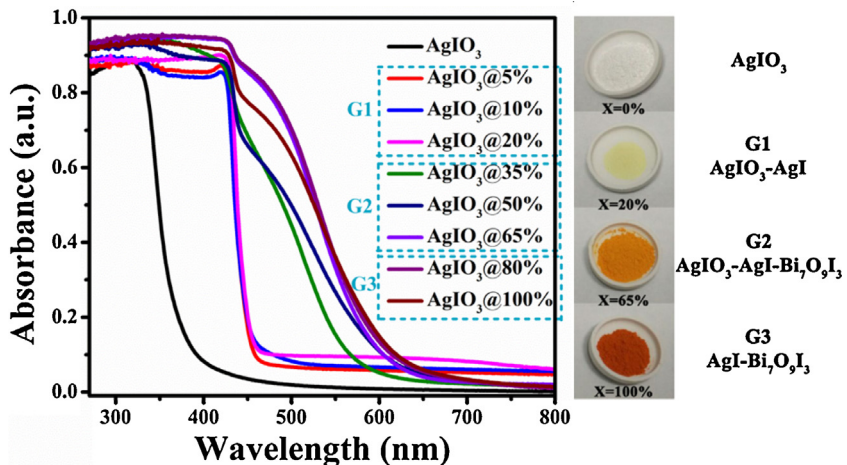


Fig. 5. DRS spectra for the AgIO₃, AgIO₃@X (X = 5%, 10%, 20%, 35%, 50%, 65%, 80%, 100%) samples, and the digital photos of the AgIO₃, AgIO₃@20% (G1, AgI/AgIO₃), AgIO₃@65% (G2, Bi₇O₉I₃/AgI/AgIO₃), and AgIO₃@100% (G3, Bi₇O₉I₃/AgI) samples.

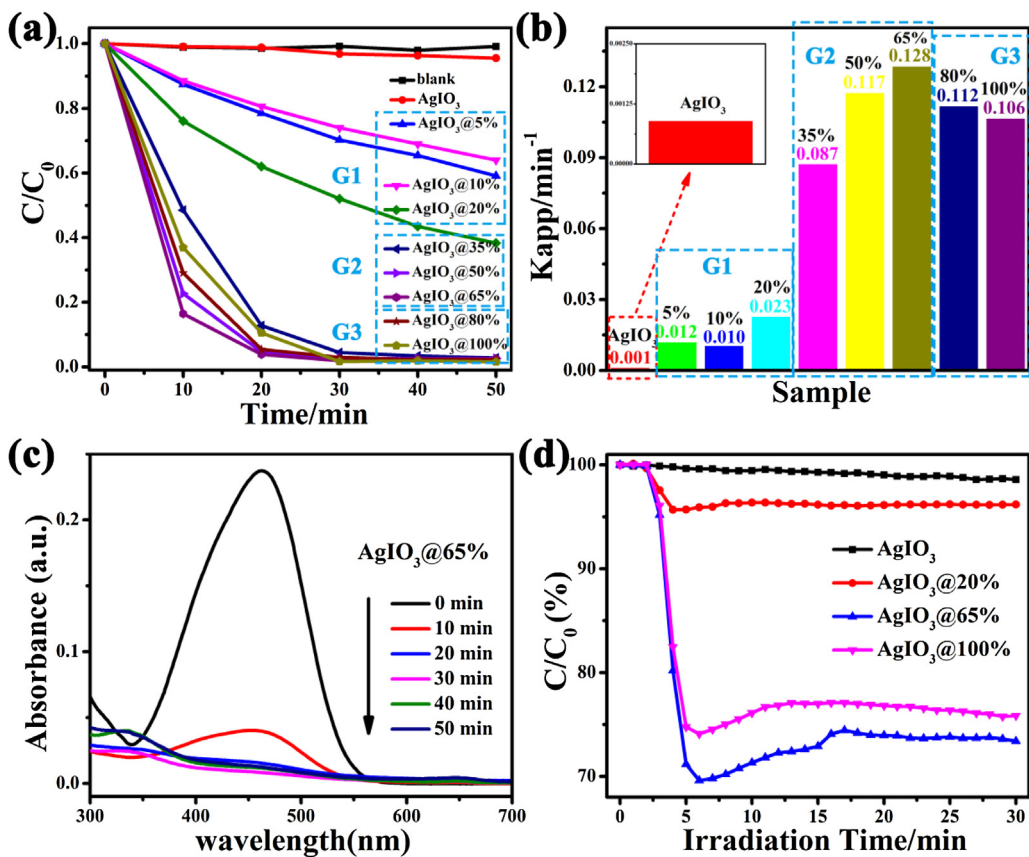


Fig. 6. Photodegradation curves of MO solution over the as-obtained AgIO₃, and three groups (G1, G2 and G3) photocatalysts under simulated solar light irradiation (a). Kinetic constants for degradation of MO over AgIO₃, and AgIO₃@X composites (b). Time-resolved absorption spectrum of MO for AgIO₃@65% (c), and Photocatalytic removal NO in air under simulated solar light irradiation (d).

concentration (mol/L) at time t , respectively. With increasing the X value from 5% to 100%, the photodegradation rate constant of AgIO₃@X approximately ascends at first and reaches the maximum of 0.128 min⁻¹ at AgIO₃@65% (G2, Bi₇O₉I₃/AgI/AgIO₃), which is 128, 5.57, and 1.21 times higher than those of AgIO₃ (0.001 min⁻¹), AgIO₃@20% (0.023 min⁻¹, G1, AgI/AgIO₃), and AgIO₃@100% (0.106 min⁻¹, G3, Bi₇O₉I₃/AgI), and then decreases with further increasing X value. The rate constant of AgIO₃@10% (0.010 min⁻¹) is lower than that of AgIO₃@5% (0.012 min⁻¹) and AgIO₃@20% (0.023 min⁻¹), which can be explained as follows: In

AgIO₃@5%, a small amount of AgI is produced and a synergistic effect is realized between AgI and AgIO₃. In AgIO₃@20%, there were so much AgI produced that AgI plays a more dominant role than AgIO₃ in the degradation process. However, the amount of AgI generated in AgIO₃@10% was more than that in AgIO₃@5%, which inhibited the synergistic effect between AgIO₃ and AgI. Therefore, AgIO₃@10% displays weaker photocatalytic activity than AgIO₃@5% and AgIO₃@20%. Fig. S4 and Fig. 6c shows time-resolved absorption spectra of MO for AgIO₃, and AgIO₃@65%, respectively. In Fig. S4, with prolonging simulated solar irradiation, little MO is degraded

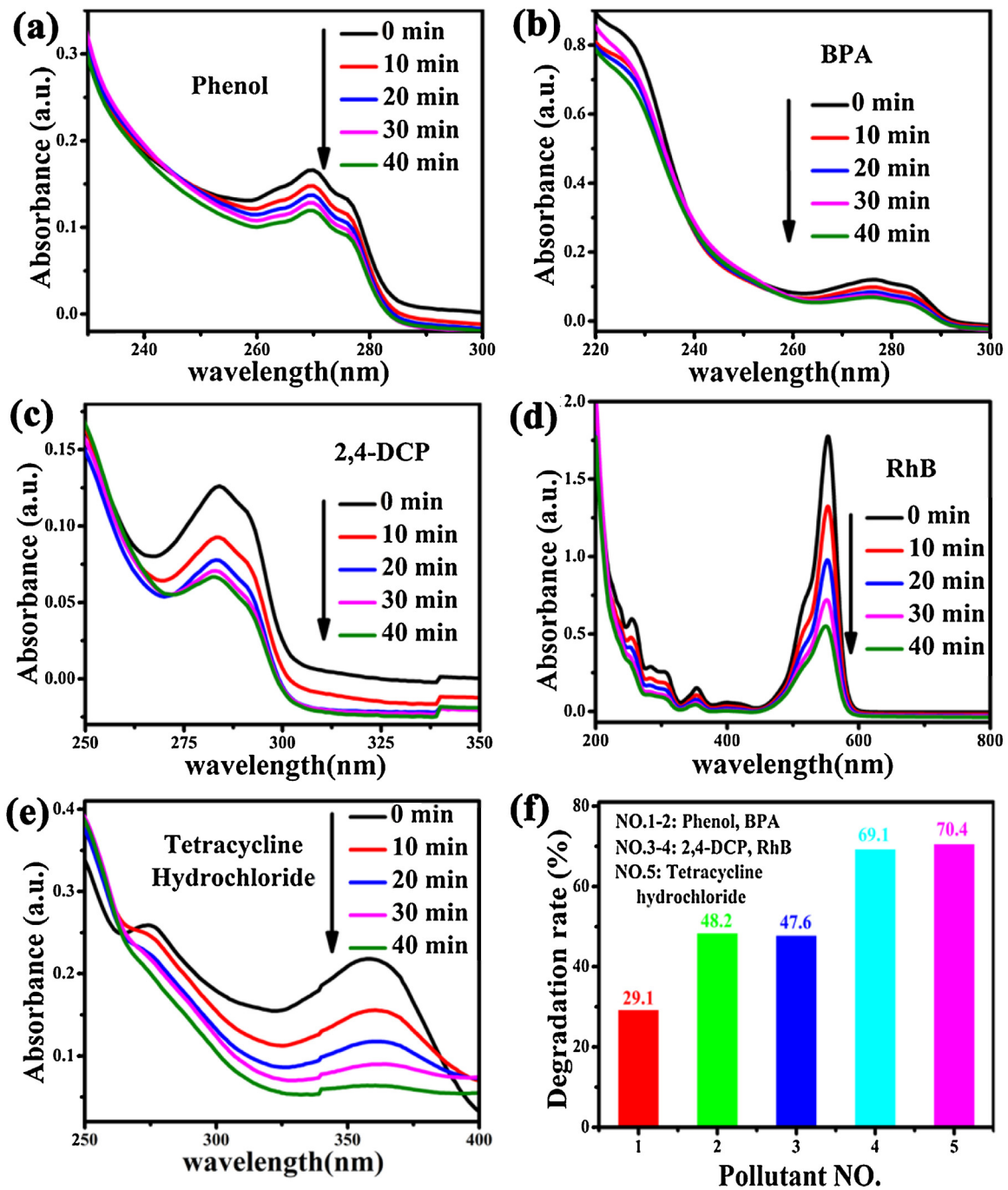


Fig. 7. UV-vis absorption spectra of Phenol (a), BPA (b), 2,4-DCP (c), RhB (d), tetracycline hydrochloride (e) over $\text{AgI}/\text{O}_3@65\%$ (G2, $\text{Bi}_7\text{O}_9\text{I}_3/\text{AgI}/\text{AgI}/\text{O}_3$) under simulated solar light irradiation. Degradation rate of diverse pollutants after 40 min simulated solar light irradiation (f).

by AgI/O_3 . But most of MO has been degraded by $\text{AgI}/\text{O}_3@65\%$ after simulated solar light irradiation for 50 min (Fig. 6c). Based on the previous reports [38,39], the possible photodegradation products of MO are 4-amino sulfonic acid and N,N-dimethyl-*p*-phenylenediamine.

Furthermore, we also test the photocatalytic activity of AgI/O_3 , $\text{AgI}/\text{O}_3@20\%$ (G1, $\text{AgI}/\text{AgI}/\text{O}_3$), $\text{AgI}/\text{O}_3@65\%$ (G2, $\text{Bi}_7\text{O}_9\text{I}_3/\text{AgI}/\text{AgI}/\text{O}_3$), and $\text{AgI}/\text{O}_3@100\%$ (G3, $\text{Bi}_7\text{O}_9\text{I}_3/\text{AgI}$) photocatalysts by photodecolorizing MO under visible light irradiation ($\lambda > 420$ nm). From Fig. S5(a) and (b), the $\text{AgI}/\text{O}_3@65\%$ sample exhibits the best photocatalytic activity in the four sample. Meanwhile, the composite photocatalysts ($\text{AgI}/\text{O}_3@20\%$, $\text{AgI}/\text{O}_3@65\%$, and $\text{AgI}/\text{O}_3@100\%$) display much better photocatalytic performance than that of AgI/O_3 precur-

sor, which is consistent well with their activity order in the above degradation experiments under simulated solar light.

3.3.2. Photodegradation of NO

NO, a stubborn gaseous pollutant can be removed by photolysis process. We herein photo-catalyze NO to monitor the photocatalytic activity of AgI/O_3 , $\text{AgI}/\text{O}_3@20\%$ ($\text{AgI}/\text{AgI}/\text{O}_3$), $\text{AgI}/\text{O}_3@65\%$ ($\text{Bi}_7\text{O}_9\text{I}_3/\text{AgI}/\text{AgI}/\text{O}_3$), and $\text{AgI}/\text{O}_3@100\%$ ($\text{Bi}_7\text{O}_9\text{I}_3/\text{AgI}$) samples under simulated solar light irradiation. As shown in Fig. 6d, after 30 min simulated solar light irradiation, the NO removal rate of $\text{AgI}/\text{O}_3@65\%$ can reach 27.6%, which excels AgI/O_3 (1.42%), $\text{AgI}/\text{O}_3@20\%$ (4.05%), and $\text{AgI}/\text{O}_3@100\%$ (24.2%). In addition, both $\text{AgI}/\text{O}_3@65\%$ and $\text{AgI}/\text{O}_3@100\%$ exhibit much higher photocatalytic

ability than AgIO_3 @20%, which should be ascribed to the existence of $\text{Bi}_7\text{O}_9\text{I}_3$. The NO removal result is strictly consistent with the above MO degradation results.

3.3.3. Photodegradation of diverse pollutants

To further investigate the strong photooxidation capability of multi-phase heterojunction, the photocatalytic activity of AgIO_3 @65% ($\text{Bi}_7\text{O}_9\text{I}_3/\text{AgI}/\text{AgIO}_3$) is also explored through photodecomposition of diverse industrial pollutants and pharmaceuticals, such as phenol, 2,4-dichlorophenol (2,4-DCP), bisphenol A (BPA), and tetracycline hydrochloride. These contaminants and pharmaceuticals can induce tissue necrosis or other serious adverse effects for human health [40]. Fig. 7a–e exhibits the time-resolved UV-vis absorption spectra of phenol, BPA, 2,4-DCP, RhB, and tetracycline hydrochloride over AgIO_3 @65% under simulated solar light irradiation. It was seen that all these contaminants can be destroyed by AgIO_3 @65%, and the degradation rate reaches 29.1%, 48.2%, 47.6%, 69.1% and 70.4% for phenol, BPA, 2,4-DCP, RhB and tetracycline hydrochloride, respectively, with simulated solar light irradiation for 40 min, as shown in Fig. 7f. These results demonstrate the superior photocatalytic activity of AgIO_3 @65% ($\text{Bi}_7\text{O}_9\text{I}_3/\text{AgI}/\text{AgIO}_3$), which holds huge potentials for practical application in environmental remediation.

3.3.4. Stability of photocatalyst

To evaluate the stability of the as-prepared photocatalysts, five-cycle recycling experiments is performed over AgIO_3 @65% photocatalyst. As shown in Fig. S6, the photocatalytic activity has almost no big loss. Moreover, the XRD and XPS pattern (Fig. S7–S8) of AgIO_3 @65% also have no obvious change between before and after photoreaction. All these results reveal the high stability of AgIO_3 @65%.

3.3.5. Charge separation and photocatalytic enhancement mechanism

Generally, low recombination rate of photogenerated charge carrier means a better photocatalytic activity [41]. To investigate the separation efficiency of photogenerated holes and electrons in photocatalysts, the photoluminescence spectra (PL) and electrochemical impedance spectra (EIS) are carried out. The PL spectra of pristine AgIO_3 and three groups of composite photocatalysts are shown in Fig. 8a. It can be found that the PL spectra of samples in G1 are similar to that of AgIO_3 , but the spectra of samples in G2 and G3 are quite different due to the existence of new phase $\text{Bi}_7\text{O}_9\text{I}_3$ in samples of G2 and G3. With increasing the value of X, the photoluminescence emission peak gradually shifts to high wavelength, which is coinciding with the continuous red-shift of the photoabsorption of composites. Lower PL emission intensity usually indicates a lower recombination rate of photoinduced electron-hole pairs [42]. Therefore, it can be deduced that the fabrication of heterojunction can restrain the recombination rate of photogenerated electrons and holes and improve the photocatalytic activity of composite photocatalysts. The EIS Nyquist plots of AgIO_3 , AgIO_3 @20% (AgI/AgIO_3), AgIO_3 @65% ($\text{Bi}_7\text{O}_9\text{I}_3/\text{AgI}/\text{AgIO}_3$), and AgIO_3 @100% ($\text{Bi}_7\text{O}_9\text{I}_3/\text{AgI}$) photocatalysts have been employed to further clarify photogenerated charge transfer efficiency. In general, a smaller arc radius reflects a higher charge transfer efficiency. As shown in Fig. 8b, the arc radius order of the four samples from the biggest to smallest is AgIO_3 , AgIO_3 @20%, AgIO_3 @100%, and AgIO_3 @65%. It indicates that $\text{Bi}_7\text{O}_9\text{I}_3/\text{AgI}/\text{AgIO}_3$ possesses the highest charge transfer efficiency among the different heterojunctions. Thereby, it is corroborated that construction of heterostructure can realize the enhancement of photoexcited charge transfer and separation efficiencies.

To disclose the photocatalytic mechanism of the as-obtained photocatalysts, the reactive species ($\bullet\text{O}_2^-$, h^+ or $\bullet\text{OH}$) involved in

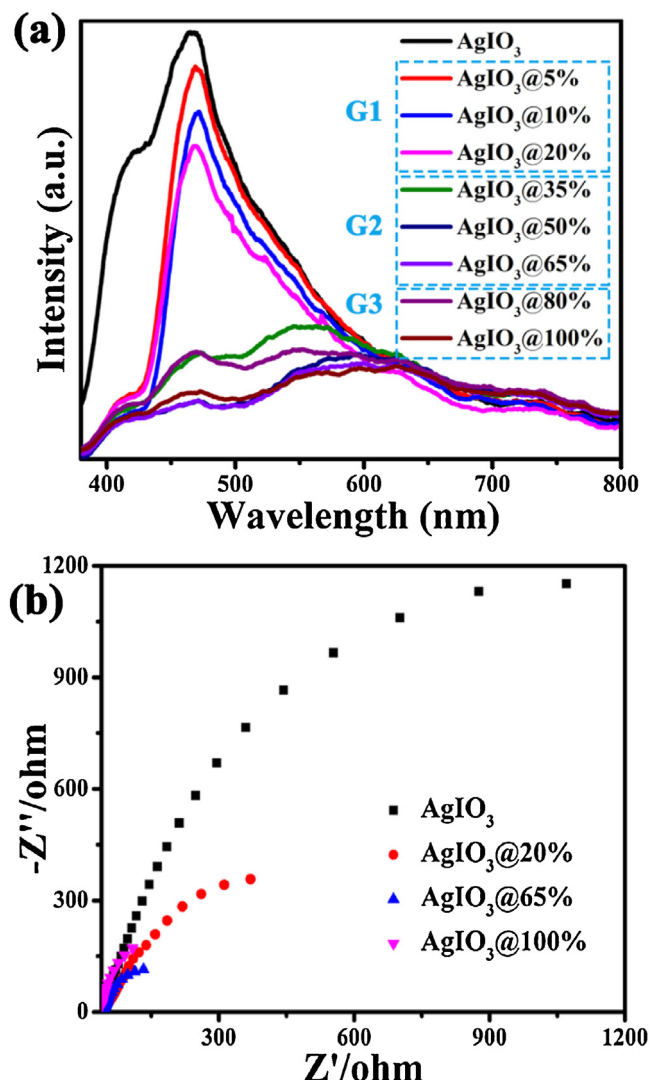


Fig. 8. Photoluminescence spectra of pure AgIO_3 , and three groups photocatalysts (G1, G2 and G3) under the excitation of 350 nm (a), and EIS Nyquist plots for AgIO_3 , AgIO_3 @20% (G1, AgI/AgIO_3), AgIO_3 @65% (G2, $\text{Bi}_7\text{O}_9\text{I}_3/\text{AgI}/\text{AgIO}_3$), and AgIO_3 @100% (G3, $\text{Bi}_7\text{O}_9\text{I}_3/\text{AgI}$) photocatalysts (b).

the photocatalytic decomposition process are detected by active species trapping experiments. Disodium ethylenediaminetetraacetate (EDTA-2Na), benzoquinone (BQ), and isopropanol (IPA) are introduced as the h^+ , $\bullet\text{O}_2^-$, and $\bullet\text{OH}$ scavengers, respectively [43]. The active species trapping experiment results for AgIO_3 @20% (AgI/AgIO_3), AgIO_3 @65% ($\text{Bi}_7\text{O}_9\text{I}_3/\text{AgI}/\text{AgIO}_3$), and AgIO_3 @100% ($\text{Bi}_7\text{O}_9\text{I}_3/\text{AgI}$) photocatalysts are displayed in Fig. 9. The reaction rates are estimated by the previous mentioned equation: $\ln(C_0/C) = k_{\text{app}}t$. For AgIO_3 @20% (AgI/AgIO_3), as shown in Fig. 9a, h^+ , $\bullet\text{O}_2^-$, and $\bullet\text{OH}$ all participate in the degradation process, and the $\bullet\text{O}_2^-$ plays a dominant role. Similarly, h^+ , $\bullet\text{O}_2^-$, and $\bullet\text{OH}$ are also critical in the degradation process of MO for AgIO_3 @65% ($\text{Bi}_7\text{O}_9\text{I}_3/\text{AgI}/\text{AgIO}_3$) (Fig. 9b). However, one can see that the inhibition effect of adding 1 mM IPA on degradation efficiency of AgIO_3 @65% is slighter than that of AgIO_3 @20%, revealing the decreased yield of $\bullet\text{OH}$ by AgIO_3 @65%. In addition, we take ammonium oxalate (AO) and *tert*-butyl alcohol (TBA) to scavenge h^+ and $\bullet\text{OH}$ in another radical scavengers experiment (Fig. S9) [44], one can see that the result is consistent with the that of the radical scavengers experiment with using EDTA-2Na and IPA as quenching agents of h^+ and $\bullet\text{OH}$. With regard to AgIO_3 @100% ($\text{Bi}_7\text{O}_9\text{I}_3/\text{AgI}$), $\bullet\text{O}_2^-$ plays a dominant role and h^+ takes a second role as shown

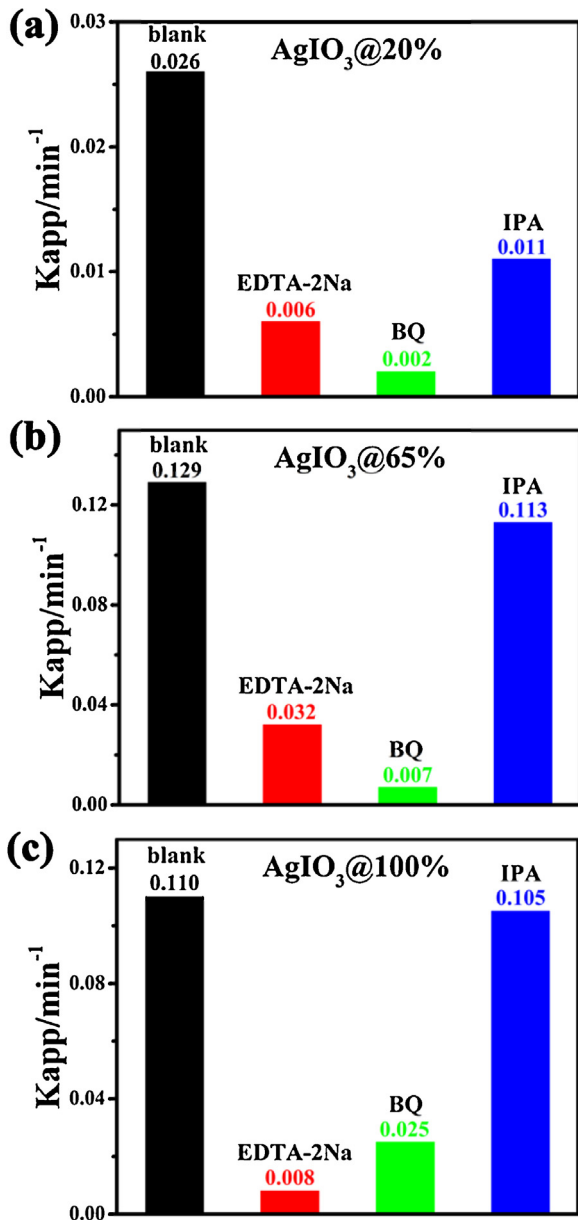


Fig. 9. Photocatalytic degradation of MO over the (a) AgIO₃@20% (G1, AgI/AgIO₃), (b) AgIO₃@65% (G2, Bi₇O₉I₃/AgI/AgIO₃), and (c) AgIO₃@100% (G3, Bi₇O₉I₃/AgI) photocatalysts alone and with the addition of different active species scavengers.

in Fig. 9c, and meanwhile the effect of •OH can be neglected because the IPA inhibition efficiency for MO degradation is as low as 4.55%. The different active species trapping experiment results among AgIO₃@20% (AgI/AgIO₃), AgIO₃@65% (Bi₇O₉I₃/AgI/AgIO₃), and AgIO₃@100% (Bi₇O₉I₃/AgI) demonstrated that diverse photocatalytic mechanisms exist in the degradation processes of the three-class photocatalysts.

The process that NO reacts with the photo-generated reactive radicals and is transformed to final NO₃⁻ can be divided as four reactions displayed in Eqs. (1)–(4) [45].

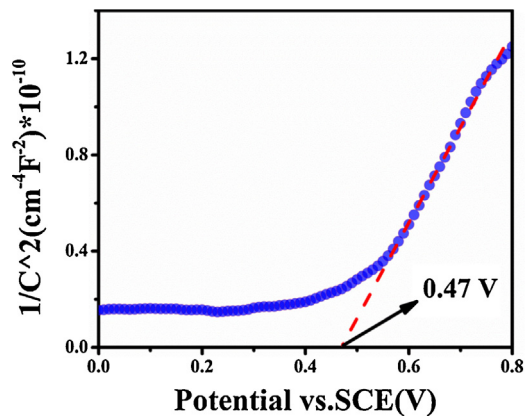
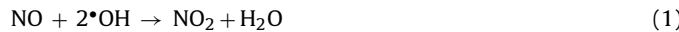


Fig. 10. Mott-Schottky curve for AgIO₃ photocatalyst (1000 Hz).

As the photocatalytic reaction was going on, the NO concentration in the outlet gradually converts to NO₃⁻.

Mott-Schottky method is used to clarify the band structure of AgIO₃, and its Mott-Schottky curve with a frequency of 1000 Hz is illustrated in Fig. 10. In general, the flat-band potential values (E_{fb}) can be calculated by using the following Mott-Schottky equation [46].

$$\frac{1}{C^2} = \frac{2}{\varepsilon \varepsilon_0 N_D} \left(E - E_{fb} - \frac{k_B T}{q} \right)$$

where ε are ε_0 the dielectric constants of free space and the film electrode, and C , E , N_D , T , k_B , and q represents the space charge capacitance, applied potential, donor density, temperature, Boltzmann's constant, and electronic charge, respectively. With intercepting the extrapolation to $1/C^2 = 0$, the flat potential (E_{fb}) of AgIO₃ is estimated to be 0.47 V versus saturated calomel electrode (SCE), which is 0.71 V versus the normal hydrogen electrode (NHE) at the same time. The positive slop of Mott-Schottky curve indicates that AgIO₃ is an *n*-type semiconductor. As shown in the literature [47], the flat potential of *n*-type semiconductor is 0.1–0.3 eV below the conduction band position, which is decided by the carrier concentration and electron effective mass. Therefore, the conduction band (CB) potential (E_{CB}) for AgIO₃ can be determined as 0.61 eV, and its valence band (VB) potential (E_{VB}) is 3.79 eV, respectively.

On the basis of band structure, different photocatalytic mechanisms over AgIO₃@20% (AgI/AgIO₃), AgIO₃@65% (Bi₇O₉I₃/AgI/AgIO₃), and AgIO₃@100% (Bi₇O₉I₃/AgI) photocatalysts are proposed and schematically displayed in Fig. 11. According to the previous report [31,48], the band energy levels of AgI and Bi₇O₉I₃ are as follows: AgI ($E_{CB} = -0.15$ eV, $E_{VB} = 2.65$ eV), and Bi₇O₉I₃ ($E_{CB} = -0.63$ eV, $E_{VB} = 1.41$ eV). For AgIO₃@20% (AgI/AgIO₃), both AgIO₃ and AgI can be excited by simulated solar light irradiation (Fig. 11a), and the electrons and holes are produced. Owing to the more positive CB of AgIO₃ (0.61 eV) compared to that of AgI (-0.15 eV), the electrons of AgI would transfer to the CB of AgIO₃. In general, the CB position of AgIO₃ (0.61 eV) is more positive than O₂/•O₂⁻ (-0.05 eV) [40], so electrons on the AgIO₃ CB are unable to reduce O₂ to produce •O₂⁻. However, a shift of the AgIO₃ fermi level could occur in actual photocatalytic system, and then the energy level and surrounding medium of AgIO₃ are rearranged as reported in the literature by He *et al.* [19]. Therefore, the electrons from AgIO₃ can reduce CO₂ to CH₄ and CO, though the CO₂/CO and CO₂/CH₄ redox potentials are -0.53 and -0.24 eV. Subsequently, the electrons on the CB of AgIO₃ can reduce oxygen molecular to •O₂⁻, and the holes of AgIO₃ would transfer to the more negative VB of AgI. Compared to the potentials of •OH/H₂O (2.27 eV) and •OH/OH⁻ (1.99 eV) [40], the VB potential of AgI (2.6 eV) is positive enough to generate another powerful radical •OH via the reaction

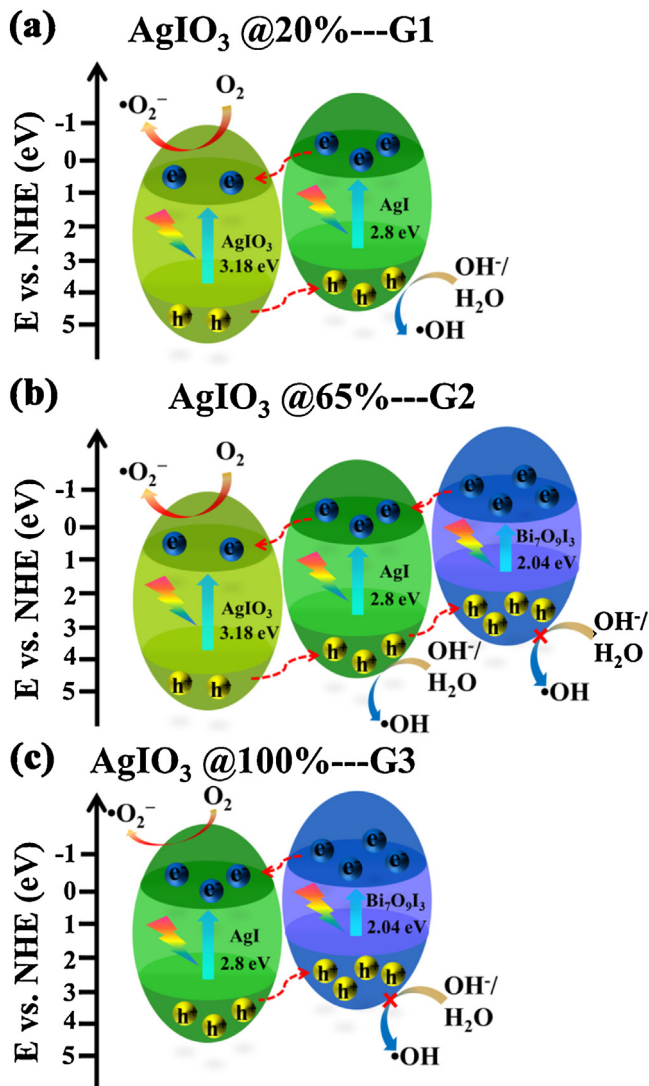


Fig. 11. The proposed photocatalytic mechanisms over: (a) $\text{AgIO}_3@20\%$ (G1, AgI/AgIO_3), (b) $\text{AgIO}_3@65\%$ (G2, $\text{Bi}_7\text{O}_9\text{I}_3/\text{AgI}/\text{AgIO}_3$), and (c) $\text{AgIO}_3@100\%$ (G3, $\text{Bi}_7\text{O}_9\text{I}_3/\text{AgI}$) photocatalysts.

between $\text{H}_2\text{O}/\text{OH}^-$ and h^+ . For $\text{AgIO}_3@20\%$ (AgI/AgIO_3), the amount of AgIO_3 is more than that of AgI , which favors generation of more $\bullet\text{O}_2^-$ than holes to participate in the photocatalytic process [43]. That is why $\bullet\text{O}_2^-$ plays a dominant role in this system. As for $\text{AgIO}_3@65\%$ ($\text{Bi}_7\text{O}_9\text{I}_3/\text{AgI}/\text{AgIO}_3$), $\text{Bi}_7\text{O}_9\text{I}_3$ plays a significant part. As $\text{Bi}_7\text{O}_9\text{I}_3$ absorbs intensive visible light (400–650 nm), much more electron-hole pairs are produced from $\text{Bi}_7\text{O}_9\text{I}_3$ as shown in Fig. 11b. These robust electrons produced from $\text{Bi}_7\text{O}_9\text{I}_3$ and AgI would transfer to the CB of AgIO_3 to be $\bullet\text{O}_2^-$. On the other hand, a majority of holes from AgIO_3 and AgI would transfer to the VB of $\text{Bi}_7\text{O}_9\text{I}_3$ (1.41 eV). As it is more negative than $\bullet\text{OH}/\text{H}_2\text{O}$ (2.27 eV) and $\bullet\text{OH}/\text{OH}^-$ (1.99 eV), $\bullet\text{OH}$ cannot almost be generated. Whereas, seen from the active species trapping experiments that $\bullet\text{OH}$ also works in this degradation process, which may be resulted from the small number of holes staying in the VB of AgI . Due to relatively large amount of AgIO_3 , $\bullet\text{O}_2^-$ is still the main active species in this system. With regard to $\text{AgIO}_3@100\%$ ($\text{Bi}_7\text{O}_9\text{I}_3/\text{AgI}$), AgIO_3 almost all converts to AgI , leaving the two active components AgI and $\text{Bi}_7\text{O}_9\text{I}_3$ (Fig. 11c). The electrons of $\text{Bi}_7\text{O}_9\text{I}_3$ transfer to AgI CB and holes of AgI transfer to $\text{Bi}_7\text{O}_9\text{I}_3$ VB. The CB potential of AgI (-0.15 eV) is more negative than $\text{O}_2/\bullet\text{O}_2^-$ (-0.05 eV), so the electrons in AgI CB can reduce oxygen molecular to be $\bullet\text{O}_2^-$ radicals. In this system,

$\bullet\text{O}_2^-$ plays a dominant role and h^+ comes next in MO degradation process because the amount of $\text{Bi}_7\text{O}_9\text{I}_3$ is larger than that of AgI on account of I XPS spectra. Because $\text{AgIO}_3@65\%$ ($\text{Bi}_7\text{O}_9\text{I}_3/\text{AgI}/\text{AgIO}_3$) contains the narrow-band-gap $\text{Bi}_7\text{O}_9\text{I}_3$, substantial photoexcited charge carriers could be produced. Meanwhile, it holds a three-rank heterojunctional structure with well-aligned energy levels, where the separation and transfer of electrons and holes can be significantly facilitated. Thus, $\text{AgIO}_3@65\%$ possesses the outstanding photocatalytic activity compared to other two types of heterojunction. The three-group heterojunctions possess diverse photocatalytic mechanisms, which are closely related with their components. The high photoabsorption and well-matched band structure are well balanced and optimized in $\text{Bi}_7\text{O}_9\text{I}_3/\text{AgI}/\text{AgIO}_3$.

4. Conclusions

In summary, three classes of heterojunction photocatalysts AgI/AgIO_3 , $\text{Bi}_7\text{O}_9\text{I}_3/\text{AgI}/\text{AgIO}_3$ and $\text{Bi}_7\text{O}_9\text{I}_3/\text{AgI}$ were synthesized via a facile one-step *in-situ* treatment using AgIO_3 as self-sacrifice precursor at room temperature. The visible-light absorption and photocatalytic activity of AgIO_3 is greatly promoted due to the heterostructure formation between different phases in composite photocatalysts. The ternary heterojunction $\text{Bi}_7\text{O}_9\text{I}_3/\text{AgI}/\text{AgIO}_3$ exhibits the best photocatalytic activity in photodegrading methyl orange (MO) and NO gas removal under simulated solar light irradiation. Notably, $\text{Bi}_7\text{O}_9\text{I}_3/\text{AgI}/\text{AgIO}_3$ also shows powerful photocatalytic performance for decomposition of diverse industrial contaminants and pharmaceutical, including, RhB, phenol, 2,4-DCP, BPA, and tetracycline hydrochloride. Systematic investigations on charge transfer and active species reveal that the three groups of composite photocatalysts have different photocatalytic mechanisms with discrepant charge separation efficiency, accounting for their distinct photocatalytic activity. The present work opens a new route for preparation of component-adjustable heterostructural photocatalysts with excellent photocatalytic performance.

Acknowledgements

This work was supported by the National Natural Science Foundations of China (Grant No. 51302251 and 51372233), the Fundamental Research Funds for the Central Universities (No. 2652013052, 2652015296, 2652015439).

Appendix A. Supplementary data

Supplementary data associated with this article can be found, in the online version, at <http://dx.doi.org/10.1016/j.apcatb.2016.04.036>.

References

- [1] H.W. Huang, Y. He, Z.S. Lin, L. Kang, Y.H. Zhang, *J. Phys. Chem. C* 117 (2013) 22986–22994.
- [2] J. Jiang, L.Z. Zhang, H. Li, W.W. He, J.J. Yin, *Nanoscale* 5 (2013) 10573–10581.
- [3] N. Zhang, M.Q. Yang, S.Q. Liu, Y.G. Sun, Y.J. Xu, *Chem. Rev.* 115 (2015) 10307–10377.
- [4] D.F. Xu, B. Cheng, J.F. Zhang, W.K. Wang, J.G. Yu, W.K. Ho, *J. Mater. Chem. A* 3 (2015) 20153–20166.
- [5] Y.P. Bi, H.Y. Hu, S.X. Ouyang, Z.B. Jiao, G.X. Lu, J.H. Ye, *J. Mater. Chem. A* 22 (2012) 14847–14850.
- [6] C. Han, M.Q. Yang, B. Weng, Y.J. Xu, *Phys. Chem. Chem. Phys.* 16 (2014) 16891–16903.
- [7] Y.H. Zhang, Z.R. Tang, X.Z. Fu, Y.J. Xu, *ACS Nano* 4 (2010) 7303–7311.
- [8] D.L. Jiang, L.L. Chen, J.J. Zhu, M. Chen, W.D. Shi, J.M. Xie, *Dalton Trans.* 42 (2013) 15726–15734.
- [9] Y.H. Zhang, Z.R. Tang, X.Z. Fu, Y.J. Xu, *Appl. Catal. B* 106 (2011) 445–452.
- [10] Q. Zhu, W.S. Wang, L. Lin, G.Q. Gao, H.L. Guo, H. Du, A.W. Xu, *J. Phys. Chem. C* 117 (2013) 5894–5900.
- [11] R. Qiao, M.M. Mao, E.L. Hu, Y.J. Zhong, J.Q. Ning, Y. Hu, *Inorg. Chem.* 54 (2015) 9033–9039.

- [12] S.W. Zhang, J.X. Li, X.K. Wang, Y.S. Huang, M.Y. Zeng, J.Z. Xu, *ACS Appl. Mater. Interfaces* 6 (2014) 22116–22125.
- [13] X.F. Yang, Z.P. Chen, J.S. Xu, H. Tang, K.M. Chen, Y. Jiang, *ACS Appl. Mater. Interfaces* 7 (2015) 15285–15293.
- [14] W.J. Wang, H.F. Cheng, B.B. Huang, X.R. Li, X.Y. Qin, X.Y. Zhang, Y. Dai, *Inorg. Chem.* 53 (2014) 4989–4993.
- [15] H.W. Huang, Y. He, R. He, Z.S. Lin, Y.H. Zhang, S.C. Wang, *Inorg. Chem.* 53 (2014) 8114–8119.
- [16] H.W. Huang, Y. He, R. He, X.X. Jiang, Z.S. Lin, Y.H. Zhang, S.C. Wang, *Inorg. Chem. Comm.* 40 (2014) 215–219.
- [17] H.W. Huang, L.Y. Liu, Y.H. Zhang, N. Tian, *J. Alloy Compd.* 619 (2015) 807–811.
- [18] H.W. Huang, Y. He, Y.X. Guo, R. He, Z.S. Lin, Y.H. Zhang, *Solid State Sci.* 46 (2015) 37–42.
- [19] Z.Q. He, D. Wang, H.Y. Fang, J.M. Chen, S. Song, *Nanoscale* 6 (2014) 10540–10544.
- [20] Y.P. Bi, H.Y. Hu, S.X. Ouyang, Z.B. Jiao, G.X. Lu, J.H. Ye, *J. Mater. Chem.* 22 (2012) 14847–14850.
- [21] G.P. Dai, J.G. Yu, G. Liu, *J. Phys. Chem. C* 116 (2012) 15519–15524.
- [22] S.M. Wang, D.L. Li, C. Sun, S.G. Yang, Y. Guan, H. He, *Appl. Catal. B: Environ.* 144 (2014) 885–892.
- [23] G.Q. Luo, X.J. Jiang, M.J. Li, Q. Shen, L.M. Zhang, H.G. Yu, *ACS Appl. Mater. Interfaces* 5 (2013) 2161–2168.
- [24] Y.S. Lee, H.J. Lee, W.S. Choi, *Langmuir* 30 (2014) 9584–9590.
- [25] L. Chen, R. Huang, M. Xiong, Q. Yuan, J. He, J. Jia, M.Y. Yao, S.L. Luo, C.T. Au, S.F. Yin, *Inorg. Chem.* 52 (2013) 11118–11125.
- [26] X. Xiao, C.L. Xing, G.P. He, X.X. Zuo, J.M. Nan, L.S. Wang, *Appl. Catal. B: Environ.* 148 (2014) 154–163.
- [27] X. Xiao, R. Hao, X.X. Zuo, J.M. Nan, L.S. Lia, W.D. Zhang, *Chem. Eng. J.* 209 (2012) 293–300.
- [28] Y.G. Yu, G. Chen, X. Wang, D.C. Jia, P.X. Tang, C.D. Lv, *RSC Adv.* 5 (2015) 74174–74179.
- [29] L.M. Sun, L. Xiang, X. Zhao, C.J. Jia, J. Yang, Z. Jin, X.F. Cheng, W.L. Fan, *ACS Catal.* 5 (2015) 3540–3551.
- [30] X. Xiao, C. Liu, R.P. Hu, X.X. Zuo, J.M. Nan, L.S. Li, L.S. Wang, *J. Mater. Chem.* 22 (2012) 22840–22843.
- [31] M.C. Long, P.D. Hu, H.D. Wu, J. Cai, B.H. Tan, B.X. Zhou, *Appl. Catal. B: Environ.* 184 (2016) 20–27.
- [32] Q.C. Liu, D.K. Ma, Y.Y. Hu, Y.W. Zeng, S.M. Huang, *ACS Appl. Mater. Interfaces* 5 (2013) 11927–11934.
- [33] F. Dong, Q.Y. Li, Y.J. Sun, W.K. Ho, *ACS Catal.* 4 (2014) 4341–4350.
- [34] S.X. Yu, H.W. Huang, F. Dong, M. Li, N. Tian, T.R. Zhang, Y.H. Zhang, *ACS Appl. Mater. Interfaces* 7 (2015) 27925–27933.
- [35] M.C. Long, P.D. Hu, H.D. Wu, Y.Y. Chen, B.H. Tan, W.M. Cai, *J. Mater. Chem. A* 3 (2015) 5592–5598.
- [36] H.W. Huang, X.W. Li, J.J. Wang, F. Dong, P.K. Chu, T.R. Zhang, Y.H. Zhang, *ACS Catal.* 5 (2015) 4094–4103.
- [37] C.Y. Liu, H.W. Huang, X. Du, T.R. Zhang, N. Tian, Y.X. Guo, Y.H. Zhang, *J. Phys. Chem. C* 119 (2015) 17156–17165.
- [38] G.K. Parshtettia, A.A. Telkeb, D.C. Kalyanib, S.P. Govindwar, *J. Hazard. Mater.* 176 (2010) 503–509.
- [39] M. Sun, D.Z. Li, W.J. Li, Y.B. Chen, Z.X. Chen, Y.H. He, X.Z. Fu, *J. Phys. Chem. C* 112 (2008) 18076–18081.
- [40] H.W. Huang, Y. He, X.W. Li, M. Li, C. Zeng, F. Dong, X. Du, T.R. Zhang, Y.H. Zhang, *J. Mater. Chem. A* 3 (2015) 24547–24556.
- [41] H.W. Huang, X.W. Li, X. Han, N. Tian, Y.H. Zhang, T.R. Zhang, *Phys. Chem. Chem. Phys.* 17 (2015) 3673–3679.
- [42] J.S. Xu, T. Brenner, Z.P. Chen, D. Neher, M. Antonietti, M. Shalom, *ACS Appl. Mater. Interfaces* 6 (2014) 16481–16486.
- [43] H.W. Huang, X. Han, X.W. Li, S.C. Wang, P.K. Chu, Y.H. Zhang, *ACS Appl. Mater. Interfaces* 7 (2015) 482–492.
- [44] Y.H. Zhang, N. Zhang, Z.R. Tang, Y.J. Xu, *Chem. Sci.* 4 (2013) 1820–1824.
- [45] Z.H. Ai, W.K. Ho, S.C. Lee, L.Z. Zhang, *Environ. Sci. Technol.* 43 (2009) 4143–4150.
- [46] A.W. Bott, *Curr. Sep.* 17 (1998) 87–91.
- [47] N. Tian, H.W. Huang, C.Y. Liu, F. Dong, T.R. Zhang, X. Du, S.X. Yu, Y.H. Zhang, *J. Mater. Chem. A* 3 (2015) 17120–17129.
- [48] Y.P. Bi, S.X. Ouyang, J.Y. Cao, J.H. Ye, *Phys. Chem. Chem. Phys.* 13 (2011) 10071–10075.